

PAPER • OPEN ACCESS

## The effect of plasma shaping on high density H-mode SOL profiles and fluctuations in TCV







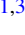





To cite this article: A. Stagni *et al* 2024 *Nucl. Fusion* **64** 026016

View the [article online](#) for updates and enhancements.

### You may also like

- [Influence of triangularity on the plasma response to resonant magnetic perturbations](#)  
S. Gu, C. Paz-Soldan, Y.Q. Liu et al.
- [NOVAE WITH LONG-LASTING SUPERSOFT EMISSION THAT DRIVE A HIGH ACCRETION RATE](#)  
Bradley E. Schaefer and Andrew C. Collazzi
- [A High-resolution Mosaic of the Neutral Hydrogen in the M81 Triplet](#)  
W. J. G. de Blok, Fabian Walter, Annette M. N. Ferguson et al.

# The effect of plasma shaping on high density H-mode SOL profiles and fluctuations in TCV

A. Stagni<sup>1,2,\*</sup> , N. Vianello<sup>1,3</sup> , M. Agostini<sup>1,3</sup> , C. Colandrea<sup>4</sup>, S. Gorno<sup>4</sup> , B. Labit<sup>4</sup> , U. Sheikh<sup>4</sup> , L. Simons<sup>4</sup>, G. Sun<sup>4</sup>, C.K. Tsui<sup>5</sup>, M. Ugoletti<sup>1,3</sup> , Y. Wang<sup>4</sup> , C. Wüthrich<sup>4</sup> , J.A. Boedo<sup>6</sup> , H. Reimerdes<sup>4</sup> , C. Theiler<sup>4</sup>  and the TCV Team<sup>a</sup>

<sup>1</sup> Consorzio RFX (CNR, ENEA, INFN, Università di Padova, Acciaierie Venete SpA), Corso Stati Uniti 4, 35127 Padova, Italy

<sup>2</sup> CRF—University of Padova, Padova, Italy

<sup>3</sup> Istituto per la Scienza e la Tecnologia dei Plasmi, CNR, Padova, Italy

<sup>4</sup> Ecole Polytechnique Fédérale de Lausanne (EPFL), Swiss Plasma Center (SPC), CH-1015 Lausanne, Switzerland

<sup>5</sup> Sandia National Laboratories, 3550 General Atomics Court 15-114A, San Diego, CA 92121, United States of America

<sup>6</sup> University of California San Diego, Center for Energy Research, La Jolla, CA 92093, United States of America

E-mail: [adriano.stagni@igi.cnr.it](mailto:adriano.stagni@igi.cnr.it)

Received 19 September 2023, revised 7 December 2023

Accepted for publication 3 January 2024

Published 12 January 2024



CrossMark

## Abstract

The impact of plasma shaping on the properties of high density H-mode scrape-off layer (SOL) profiles and transport at the outer midplane has been investigated on Tokamak configuration variable. The experimental dataset has been acquired by evolving the upper triangularity while keeping the other parameters constant. The scan comprises  $\delta_{\text{up}}$  values between 0.0 and 0.6, excluding negative triangularity scenarios. Within this study, a transition from type-I edge localised modes to the *quasi-continuous exhaust* regime takes place from low to high  $\delta_{\text{up}}$ . The modification of the upstream SOL profiles has been assessed, in terms of separatrix quantities, within the  $\alpha_t$  turbulence control parameter theoretical framework (Eich *et al* 2020 *Nucl. Fusion* **60** 056016). The target parallel heat load and the upstream near-SOL density profiles have been shown to broaden significantly for increasing  $\alpha_t$ . Correspondingly, in the far SOL a density shoulder formation is observed when moving from low to high  $\delta_{\text{up}}$ . These behaviours have been correlated with an enhancement of the SOL fluctuation level, as registered by wall-mounted Langmuir probes as well as the thermal helium beam diagnostic. Specifically, both the background and the filamentary-induced fluctuating parts of the first wall ion saturation current signal are larger at higher  $\delta_{\text{up}}$ , with filaments being ejected more frequently into the SOL. Comparison of two pulses at the extremes of the  $\delta_{\text{up}}$  scan range, but with otherwise same input parameters, shows that the midplane neutral pressure does not change much during the H-mode

<sup>a</sup> See Reimerdes *et al* 2022 (<https://doi.org/10.1088/1741-4326/ac369b>) for the TCV Team.

\* Author to whom any correspondence should be addressed.



Original Content from this work may be used under the terms of the [Creative Commons Attribution 4.0 licence](https://creativecommons.org/licenses/by/4.0/). Any further distribution of this work must maintain attribution to the author(s) and the title of the work, journal citation and DOI.

phase of the discharge. This indicates that indirect effects of the change in geometry, linked to first wall recycling sources, should not play a significant role. The total core radiation increases at high  $\delta_{\text{up}}$ , on account of a stronger plasma–wall interaction and resulting larger carbon impurity intake from the first wall. This is likely associated to the enhanced first wall fluctuations, as well as a smaller outer gap and the close-to-double-null magnetic topology at high shaping.

Keywords: H-mode, plasma shaping, scrape-off layer, power fall-off length, density shoulder, filaments, plasma-wall interaction

(Some figures may appear in colour only in the online journal)

## 1. Introduction

Proper management of the particle and energy exhaust in the divertor and scrape-off layer (SOL) regions of a tokamak is a fundamental requirement in view of safe operation of future nuclear fusion devices. In particular, an upper bound of  $10 \text{ MW m}^{-2}$  is currently set on the peak heat load impacting the divertor target and first wall components of ITER in stationary conditions, in order to prevent tungsten recrystallisation as well as excessive material erosion and melting [1]. A multi-machine empirical scaling in low collisionality, attached divertor conditions extrapolates a value for the outer midplane (OMP) power fall-off length  $\lambda_q \sim 1 \text{ mm}$  using ITER baseline parameters [2, 3]. The resulting stationary heat loads will likely pose a challenge to the material limits and a large fraction of the input power will have to be dissipated by adopting a scenario with at least a partially detached divertor. In addition, the high transient heat loads imposed by type-I edge localised modes (ELMs) [4] will have to be mitigated in ITER, if not fully suppressed in reactor-sized devices, so as to avoid a significant reduction of the lifetime of plasma-facing components.

In order to couple good core plasma performance and compatibility with the aforementioned power exhaust requirements, several alternative scenarios have been designed and are the subject of thorough research in present experimental tokamak devices. Among these, the *quasi-continuous exhaust* (QCE) H-mode regime [5] appears to be one of the most promising as a reactor solution. Generally achieved at high gas puff and high plasma shaping, close to the double null configuration, this regime is characterised by long stationary phases in which large type-I ELM events are replaced by much more frequent and incoherent small-amplitude bursts [6–9]. Recent studies carried out at ASDEX-Upgrade (AUG) [5, 10] and TCV [11] have shown a significant broadening of the SOL power width  $\lambda_q$  when transitioning from a type-I ELM regime to QCE at increasing separatrix density, relieving the peak target heat load. This however does not come at an excessive loss of core performance: good particle and energy confinement levels are retained, with the presence of an H-mode pedestal in both the upstream temperature and density profiles as well as a confinement factor  $H_{98(y,2)} \sim 1$ . Together with the relatively high fraction of power dissipated by volumetric radiation associated to the required high core plasma density [12], these features make QCE an attractive scenario for reactor operation.

The QCE regime is also characterised by the formation of a so called *density shoulder*, consisting in an overall increase and flattening of the density profile in the far SOL. In recent times, density shoulder formation has been observed both in L-mode and in H-mode [5, 13–22] during plasma discharges characterised by high divertor and midplane neutral pressure. Furthermore, it has been associated to an enhancement of turbulent transport across the SOL by means of bigger and radially faster intermittent filamentary structures [11] being expelled more frequently from the confined region into the far SOL [22, 23]. An enhancement of the radial convective transport around the OMP in high density H-mode regimes, such as QCE, could represent a hazard for the safety of first wall components [16, 24].

Despite the numerous efforts undertaken in the past years, a commonly accepted description of the SOL dynamics regulating the evolution of the upstream profiles and turbulence in high density H-mode regimes is still missing. According to the current understanding based on AUG and Tokamak configuration variable (TCV) experimental results (see e.g. [6, 7, 25, 26] and references therein), ballooning modes developing in the vicinity of the pedestal foot are thought to be the primary cause driving small ELMs and turbulent transport in QCE. More specifically, large separatrix density should lead to an enhancement of the transport level associated to these modes. At strong plasma shaping, in a close to double null configuration, the magnetic shear in the vicinity of the separatrix at the OMP decreases and thus also its stabilising effect on ballooning modes should be reduced. These conditions produce a plasma that is only marginally stable to ballooning modes in the close proximity of the separatrix. As a consequence of the resulting increased ballooning transport level, the local pressure profile near the separatrix flattens, leading to a narrowing of the pedestal width and therefore to a stabilisation of type-I ELMs.

From the theoretical point of view, in recent years a framework has been proposed and described in [10, 27]. Leveraging on the concept of a separatrix operational space [28] and on the Drift–Alfvén turbulence model [29, 30], this framework attempts a description of the SOL plasma properties by means of the so called turbulence control parameter

$$\alpha_t = KRq_{\text{cyl}}^2 \frac{n_{e,\text{sep}}}{T_{e,\text{sep}}^2} Z_{\text{eff}} \propto q_{\text{cyl}} \nu_{\text{ei}}^* \quad (1)$$

In equation (1),  $R$  is the tokamak major radius,  $q_{\text{cyl}}$  is the cylindrical safety factor,  $n_{\text{e,sep}}$  and  $T_{\text{e,sep}}$  are respectively the separatrix density and temperature,  $Z_{\text{eff}}$  is the effective ion charge and  $\nu_{\text{ei}}^*$  is the normalised edge collisionality. All parameters appearing in equation (1) are described in more detail in [10]. The definition of  $\alpha_t$  includes a proportionality constant  $K$  which depends on physical constants, the effective ion mass and the typical values assumed by  $Z_{\text{eff}}$  in a given machine (typically,  $K \sim 3.1 \cdot 10^{-18}$  for AUG and  $\sim 2.6 \cdot 10^{-18}$  for TCV). From a physical standpoint, the  $\alpha_t$  parameter can be regarded as a proxy for the strength of the resistive ballooning instability relative to drift wave transport near the separatrix, having been shown through simulations to set the phase shift between density and potential fluctuations [31].

Intensive experimental work has been conducted in recent years with the aim of supporting this theoretical framework. On AUG an increase in density, resulting from an increasing level of gas puffing, has led to an increase of  $\alpha_t$  and, correspondingly, a significant broadening of the SOL power channel width [5, 10]. Moreover, dedicated experimental campaigns making use of the renovated cooling water calorimetry system on AUG [32] have been carried out in order to study the response of the energy load distribution on plasma-facing components both in type-I ELMy H-mode and in QCE, finding that the fraction of the total energy deposited onto the outer limiter surface increases approximately linearly with  $\alpha_t$  [33]. In the latter work a variation of  $\alpha_t$  was induced by changing both the density through a gas fuelling scan, and the safety factor through a toroidal field scan, showing that the energy load on the limiter surface correlates better with  $\alpha_t$  than with the edge collisionality alone.

Most recently, work has started to extend the  $\alpha_t$  parameter theoretical framework to other machines. Notably, H-mode experiments have been carried out on TCV consisting in a separatrix density scan in highly shaped plasmas, probing both type-I ELMy and QCE regimes [11]. An increase in  $\alpha_t$  by means of a larger separatrix density at high divertor neutral pressure resulted once again in a broadening of the near SOL heat load and density profiles. A density shoulder was observed to progressively form in the far SOL, associated to an enhancement of the radial filamentary transport towards the first wall. No relevant insight could be gained through this database on the role of other quantities defining  $\alpha_t$ , like  $I_p$ ,  $B_t$  and plasma shaping, possibly affecting the SOL turbulent dynamics, since they were kept constant.

The purpose of this manuscript is therefore to extend the database in [11] by probing the properties of SOL profiles and fluctuations in high density H-mode regimes with respect to a modification in plasma shaping. Keeping the gas fuelling constant, a scan in upper triangularity is carried out which directly correlates to a change of the edge safety factor and hence  $\alpha_t$ . In the first place, the effect of upper triangularity on the upstream SOL profiles is assessed and translated in terms of  $\alpha_t$  variation. Particular consideration is given to the power fall-off length  $\lambda_q$ , the near-SOL density e-folding length  $\lambda_n$  and the far-SOL density shoulder amplitude. In the second part of this work the focus is shifted towards plasma-wall interaction issues, in terms of both filamentary-induced turbulent

fluctuations at the midplane and first wall recycling variation with plasma shaping.

The paper is structured as follows. Section 2 will present a review of the experimental conditions, machine setup and diagnostics considered in the present work. In section 3 the impact of plasma shaping on separatrix parameters and profile properties will be evaluated, whereas in section 4 the evolution of density fluctuations will be assessed. Section 5 will present a detailed analysis of how changes in plasma shaping can affect first wall recycling particle sources and plasma-wall interaction properties. Finally, conclusions and future developments will be outlined in section 6.

## 2. Experimental setup of the plasma shaping scan database

The TCV [34] is a medium-sized tokamak with major radius  $R = 0.88$  m, minor radius  $a = 0.25$  m and great flexibility in plasma shaping and divertor geometry thanks to its highly elongated vessel and 16 independently-powered poloidal field coils, allowing wide elongation and triangularity ranges of, respectively,  $1 \leq \kappa \leq 2.8$  and  $-0.7 \leq \delta \leq 1.0$ . Exploiting these properties, an experimental dataset has been acquired consisting in a plasma shaping scan.

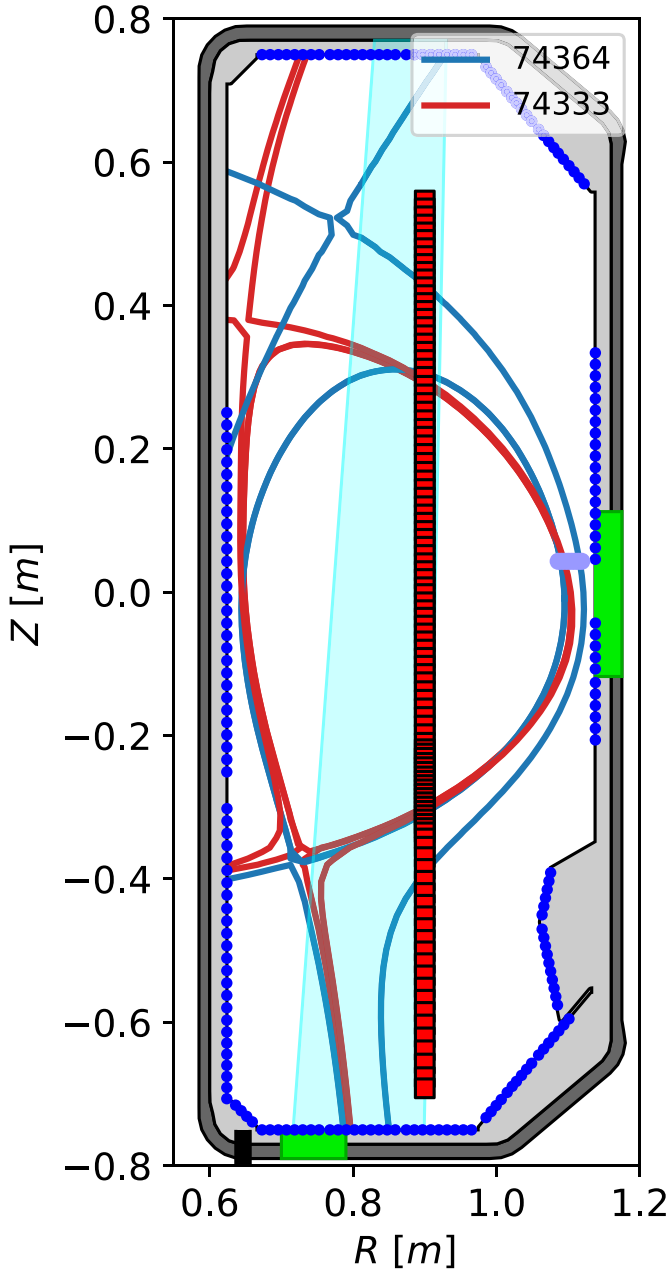
### 2.1. Machine setup and diagnostics

Figure 1 represents a poloidal cross section of the unbaffled TCV vacuum vessel and first wall, together with the full set of considered diagnostics. The outermost floor piezoelectric gas valve [35], shown as a black rectangle on the machine floor, has been used in order to puff deuterium gas in the machine. Two JET-like baratron gauges [36], shown in light green at the OMP first wall and on the vessel floor, have been used to infer the neutral pressure at different locations along the machine boundary.

The Thomson scattering (TS) system [37] is represented through red squares aligned along a vertical line of sight. It provides well-resolved spatial measurements of the temperature and density profiles across a large range of normalised minor radius, from the core plasma to the far SOL and divertor regions, with a 60 Hz time resolution. The cyan patch identifies the field of view of the vertical infrared (VIR) thermography system [38], centred around the outer strike point at  $R \sim 0.8$  m for all discharges.

The blue dots indicate the position of the wall-embedded Langmuir probes (LPs), recently upgraded in order to provide almost full coverage of the tile perimeter [39, 40]. For the majority of the considered shots they have been operated by applying a 1 kHz triangular voltage sweep, so as to infer slow density and temperature values at the first wall and divertor target. For a subset of the present database they have been instead operated at constant negative bias, yielding fast ion saturation current measurements at an acquisition frequency of 200 kHz, allowing to resolve fluctuation characteristics.

The purple dots around the outboard midplane indicate the measurement positions of the recently installed thermal



**Figure 1.** Experimental setup and diagnostics used in this work. The extent of the shaping scan is represented through two samples of the equilibria with the lowest (blue) and highest (red) upper triangularity values. Their secondary separatrices indicate their closeness to double null. The Thomson scattering volumes are represented as red dots aligned along a vertical line of sight in the vessel centre. The thermal helium beam (THB) observation points are shown as purple dots around the outer midplane. The location of the outermost floor piezoelectric valve is represented in black. The midplane and divertor baratron gauges are represented through two corresponding light green patches at the outer midplane first wall and on the vessel floor. The cyan region represents the field of view of the vertical infrared (VIR) camera, looking at a portion on the vessel floor around the outer strike point at 0.8 m. The wall-embedded Langmuir probes are represented by blue circular markers.

helium beam (THB) [41, 42], measuring the light emission of four HeI lines from a locally injected neutral helium gas cloud. By exploiting a line ratio technique, this system yields

estimates of electron density and temperature. The diagnostic observes the helium emission on eight radially spaced points, with a spatial resolution of 4.3 mm. The temporal resolution ranges from the slow evolution of the edge profiles ( $\sim 1$ – $10$  kHz) to the fast time scales associated to turbulent structures (up to 1 MHz).

## 2.2. Experimental scenario and dataset

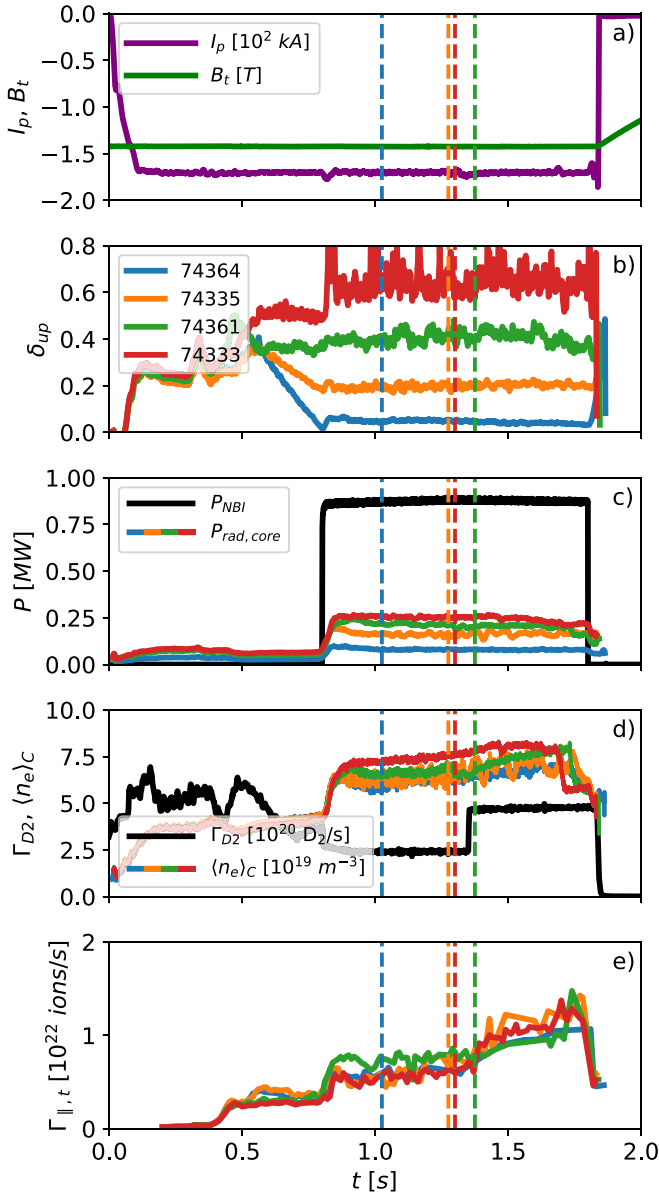
The database presented in this work is composed of high density, high recycling, deuterium-fuelled discharges performed in an unbaffled TCV vessel. The upper triangularity  $\delta_{up}$  has been changed from shot to shot, while otherwise keeping the same engineering parameters. Along with the diagnostics, figure 1 shows the extent of the present shaping scan through two samples of equilibria having, respectively, the lowest and highest upper triangularity in the dataset, together with their secondary separatrices. While the low  $\delta_{up}$  discharge consists in a lower single null, the highly shaped equilibrium is close to a double null, which is a necessary requirement for the QCE regime [7].

Figure 2 shows an overview of four representative discharges of the present plasma shaping database. As displayed in panel (a), all pulses have the same plasma current  $I_p \sim 170$  kA and central toroidal field  $B_t \sim 1.4$  T. The ion  $\nabla B$  drift is directed from the plasma towards the X-point, for easier H-mode access. The last closed flux surface (LCFS) elongation and the lower triangularity have been kept constant as well as, respectively,  $\kappa \sim 1.5$  and  $\delta_{low} \sim 0.6$ . Instead, the upper triangularity has been sampled at four approximately equally spaced values in the interval  $0.0 \lesssim \delta_{up} \lesssim 0.6$  (see panel (b)), never probing negative triangularity scenarios. This large  $\delta_{up}$  variation has allowed to cover a wide range in cylindrical safety factor  $q_{cyl}$  (as defined in [10]), with a  $\sim 27\%$  increase from  $\sim 4.4$  to  $\sim 5.6$ .

The same heating scheme has been adopted for all shapes in the form of a constant additional  $\sim 1$  MW of co-current neutral beam injection (NBI) [43] between 0.8 s and 1.8 s. The NBI heating trace is shown in panel (c) in black, together with the time evolution of the core radiated power, as measured by the RADCAM bolometry system [44], indicated by colored lines. The same flat-top fuelling scheme has been applied throughout all shots, consisting in two consecutive feed-forward gas puffing steps at  $\Gamma_{D2} \sim 2.5 \cdot 10^{20}$  mol s $^{-1}$  and  $\sim 5.0 \cdot 10^{20}$  mol s $^{-1}$  from the outermost floor piezoelectric valve. The flat-top fuelling time trace is shown in panel (d) in black, along with the time evolution of the core line-averaged density for the four selected sample discharges. The temporal trace of the total integrated inter-ELM outer target ion flux is displayed in panel (e), as measured by the floor LPs operating in swept mode. The absence of a rollover confirms that no outer target detachment occurs at this power level, even at the highest density values.

The core line averaged density across the present database covers an interval between  $\sim 6.5$  and  $\sim 8.0 \cdot 10^{19}$  m $^{-3}$ . In addition, the power radiated from the confined region spans values between  $\sim 100$  and  $\sim 200$  kW. Notably, the machine is equipped with graphite plasma-facing tiles, therefore first wall recycling particle sources around the OMP may have a rather





**Figure 2.** Time evolution of some relevant parameters for four discharges with different upper triangularity, representative of the considered plasma shaping scan. Panel (a) shows typical traces of the plasma current and the central toroidal field. Panel (b) displays the four different upper triangularity values, each associated to a colour and a sample shot number as reported in the legend. In panel (c) the NBI input power (net of beam duct losses) is shown in black, together with the core radiated power. The gas throughput from the outermost floor valve is represented in black in panel (d), together with the core line-averaged electron density. Panel (e) shows the total integrated inter-ELM outer target ion flux. The colours used for  $P_{rad,core}$  in panel (c),  $\langle n_e \rangle_C$  in panel (d) and  $\Gamma_{||,t}$  in panel (e) match those chosen in panel (b) for each different  $\delta_{up}$  value. The vertical lines indicate the centre of the time slices at which the profiles in figures 4 and 8 have been selected.

important impact on both profiles and fluctuations as the shape changes, and the outer gap along with it [19]. Furthermore, the presence of a secondary X-point close to the primary separatrix at high  $\delta_{up}$  may introduce a significant impurity source from the roof tiles. This may partly explain the differences in

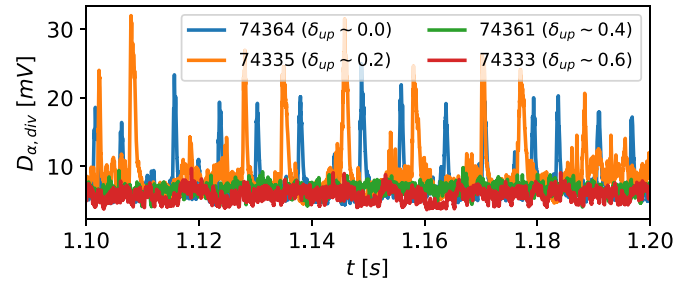


**Figure 3.** Typical ELM traces achieved within the present database at varying plasma shaping, as seen from the  $D_{\alpha}$  emission registered by a bottom-lateral photodiode line of sight. The colour coding for each temporal trace matches the one used in figure 2 to distinguish different plasma shapes.

core radiation, along with the smaller outer gap, when moving from low to high shaping. In order to improve the reproducibility of the density time evolution across the experimental program, long glow discharges have been run inter-shot. The question of possible shaping-induced variations of first wall recycling particle sources and radiative losses is addressed more in detail in section 5.

The effect of changing upper triangularity on the ELM regime is displayed in figure 3, where the time-dependent emission of  $D_{\alpha}$  light at 656 nm registered by a photodiode along a bottom-lateral line of sight is represented within a 100 ms time interval. For the two sample discharges at low shaping a type-I ELMy regime is distinctly visible in the form of large regular bursts. Conversely, a clear transition to the QCE regime takes place when moving towards highly shaped plasmas. In particular, in QCE the light emission becomes much less coherent, exhibiting a larger fluctuation level superimposed to the baseline signal with respect to type-I ELMs. This kind of ELM behaviour falls in line with previous experimental observations at AUG [6] and TCV [7].

### 3. Upstream profiles characterisation

#### 3.1. Profile analysis and methodology for separatrix parameters determination

In order to obtain a robust estimate of the separatrix electron temperature  $T_{e,sep}$  and density  $n_{e,sep}$  the approach described in [11] is used, with some minor modifications. Electron temperature and density profiles have been evaluated across the entirety of the normalised radial coordinate by means of the vertical TS system, and complemented with THB measurements in the SOL when available. Single TS profile measurements have been grouped in a steady-state time interval at least 200 ms wide during type-I ELM discharges, and subsequently filtered such that only measurements within the 65%–95% of an ELM cycle have been retained. The ELM filtering threshold bounds for the type-I ELMy cases have been chosen so that only the pre-ELM TS profiles are selected during a stationary phase of the discharge. With respect to other experimental and analysis work, done e.g. at JET [45], the inter-ELM interval

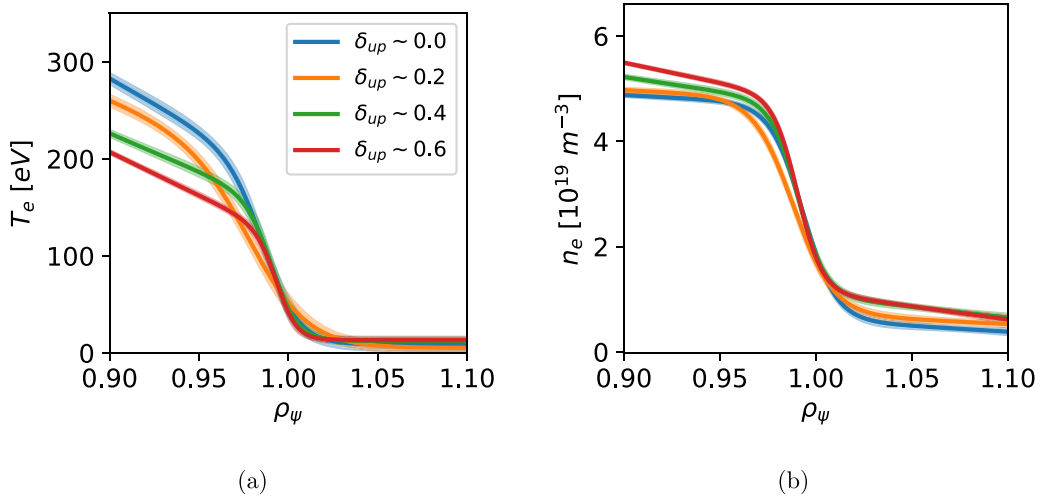


**Figure 4.** Temperature (a) and density (b) profiles for the four sample discharges shown in figure 2, one for each shape. The shown profiles have been obtained by fitting TS data only, due to the lack of THB data for this subset of the database. In order to highlight the effect on the profiles due to plasma shaping alone, the shown profiles have been selected in such a way as to have similar separatrix density. For the purpose of easier visualisation and avoidance of clustering, only the profile fits are displayed as solid lines, with their respective  $1\sigma$  uncertainty represented by the shaded areas.

width chosen here is slightly larger, for the purpose of improving the profile statistics and lowering the fitting uncertainty. During QCE phases, all profiles within a time interval of  $\sim 100$ – $150$  ms temporal width have been selected without any filtering, given the current lack of ability to properly identify separate ELMs during such regime.

All profiles have been mapped to  $\rho_\psi$ , the square root of the normalised flux coordinate, except when measuring the SOL e-folding lengths for which the physical coordinate  $R - R_{\text{sep}}$  has been used. Regularisation and fitting has been carried out by means of the analytical function described in detail in [11]. In particular, the edge and SOL regions ( $\rho_\psi \gtrsim 0.83$ ) have been characterised by means of a *modified hyperbolic tangent (mtanh)* function. A constant offset has been used for the temperature profile, whereas the density profile has been given a finite negative slope as well in the SOL. Differently from [11], only the scattering volumes below the magnetic axis have been considered instead of the whole TS line of sight as input to the fitting procedure, due to a detectable radial shift in the edge–pedestal region between the upper and lower measurements. This radial shift, which may be due to either finite poloidal gradients or uncertainties in the equilibrium reconstruction in the upper half of the machine, has already been reported in other TCV-related works (see e.g. [46]).

The radial uncertainties of the equilibrium reconstruction, coupled with the steep pedestal gradient in the edge–SOL region, represent a significant challenge to the determination of the separatrix parameters. Like in [10, 11], the position of the last-closed flux surface has been determined by means of a power balance based on the *two-point model* [47], assuming Spitzer–Härm electron heat conduction as the dominating SOL parallel transport mechanism and neglecting finite target temperature effects. All the fitted profiles are radially shifted such that the temperature at the separatrix is given by

$$T_{e,\text{sep}} \approx \left( \frac{7}{16} \frac{P_{\text{sep}} q_{\text{cyl}}^2 R}{\kappa_{0e} \hat{\kappa} a \langle \lambda_q \rangle} \right)^{2/7}, \quad (2)$$

with  $\langle \lambda_q \rangle$  evaluated as in section 3.3. The power crossing the separatrix is estimated as  $P_{\text{sep}} = P_{\text{NBI}} + P_{\text{ohm}} - P_{\text{rad,core}}$ , with  $P_{\text{NBI}}$  the coupled NBI power,  $P_{\text{ohm}}$  the ohmic heating term and  $P_{\text{rad,core}}$  the core radiative losses. A  $Z_{\text{eff}} > 1$  correction is taken into account in the electron parallel heat conductivity  $\kappa_{0e}$  [12], where  $Z_{\text{eff}}$  is a radial average of the effective ion charge estimated from the neoclassical resistivity and bootstrap current as in [48, 49]. The estimated  $T_{e,\text{sep}}$  resulting from equation (2) is of the order of  $\sim 45$  eV, similar to the values reported in [7, 50] for TCV, with a corresponding radial profile displacement of  $\sim 1.5$  mm inwards on average across the present dataset. The latter value may seem not so significant for the purpose of evaluating general trends in the profile properties at the OMP. Nonetheless, the choice of using the two-point model instead of the equilibrium reconstruction for  $T_{e,\text{sep}}$  may considerably affect the quantitative assessment of the separatrix parameters, especially when taking into account that  $\alpha_t$  shows an inverse square dependence on the separatrix temperature.

Examples of edge–SOL temperature and density profiles are shown in panels (a) and (b) of figure 4, where only the profile fits are shown without their corresponding data points in order to avoid clustering and make visualisation easier. The represented profiles, each one corresponding in colour to the sample plasma discharges shown in figure 2, have been chosen so as to be characterised by similar separatrix density ( $n_{e,\text{sep}} \sim 1.7$ – $1.8 \cdot 10^{19} \text{ m}^{-3}$ ), within experimental uncertainties. The shot numbers, upper triangularity and basic separatrix properties of the selected time slices, including their respective  $\alpha_t$  estimates, are reported in table 1. At a first glance, the two high-shaping QCE temperature profiles in figure 4(a) are

**Table 1.** Shot numbers, upper triangularity and basic separatrix properties of the selected subset of time slices within the available database, for which density and temperature profiles are shown in figures 4 and 8. For all the snapshots in the database, the major radius is  $R = 0.9$  m.

Shot #	$\delta_{up}$	$q_{cyl}$	$n_{e,sep}$ ( $m^{-3}$ )	$T_{e,sep}$ (eV)	$Z_{eff}$	$\alpha_t$
74 364	0.05	4.43	$1.86 \cdot 10^{19}$	48.1	1.60	0.61
74 335	0.17	4.80	$1.85 \cdot 10^{19}$	47.0	1.65	0.71
74 361	0.42	5.25	$1.84 \cdot 10^{19}$	45.8	1.86	1.05
74 333	0.63	5.60	$1.80 \cdot 10^{19}$	41.9	1.80	1.34

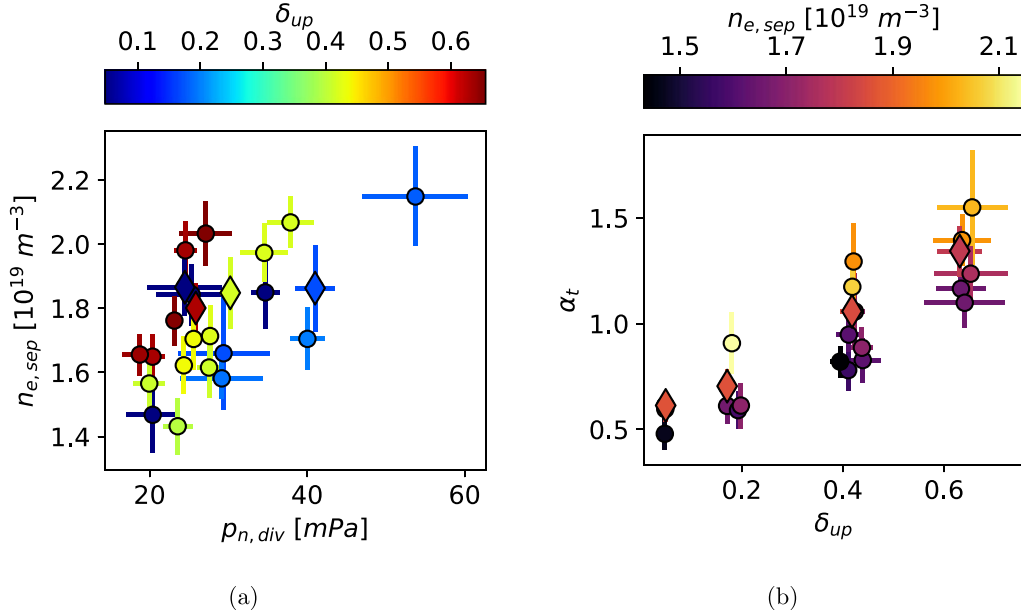


**Figure 5.** Panel (a): upstream separatrix density dependence on divertor neutral pressure and upper triangularity, respectively along the abscissa and as colormap. Panel (b): full variation of the  $\alpha_t$  parameter with upper triangularity (abscissa) and upstream separatrix density (colormap) achieved within the present dataset. In both panels, the points corresponding to the profiles shown in figures 4 and 8 are shown as large diamonds.

associated to a lower pedestal temperature than the type-I ELM ones at low shaping, whereas all fitting curves in figure 4(b) show similar pedestal density.

The latter observation seems apparently in contrast with well known experimental results [51, 52] according to which highly shaped plasmas are characterised by better pedestal confinement, owing to a higher  $n_{e,ped}$ . This is due to a strong shaping of the pedestal stability boundary at high  $\delta_{up}$  so as to include higher normalised pressure gradient and bootstrap current. However, in [45] it is noted that low pedestal collisionality is needed to explore this operational region, so that the confinement in low- and high- $\delta_{up}$  starts to branch only for  $\nu_{ped}^* \lesssim 1$ . From the respective pedestal and shaping parameters it can be calculated that the low  $\delta_{up}$  profiles in figure 4 are associated to a value of  $\nu_{ped}^* \sim 3-5$ , whereas the high  $\delta_{up}$  cases exhibit a pedestal collisionality in the range  $\sim 10-15$ . Since the pedestal density is quite similar at  $\sim 4.3 \cdot 10^{19} m^{-3}$  for all the displayed profile fits, the experimental results appear to be in line with the interpretation in [45]. Regarding  $T_{e,ped}$  instead, a significant drop is registered only for the two QCE cases, coherently with the expected lower confinement level generally observed in this regime.

### 3.2. Separatrix density and $\alpha_t$ experimental ranges

Globally across the whole shaping scan database, in figure 5(a) the expected  $n_{e,sep}$  increasing trend with the divertor neutral pressure observed in [11] is recovered when considering each plasma shape separately. In this figure, as well as in figures 5(b), 6 and 9, the large diamonds indicate the profiles displayed previously in figure 4. The  $p_{n,div}$  variation reported here is more limited when compared to the previous fuelling scan results in [11]. In the present experiments, the observed variation of the divertor neutral pressure is most likely correlated, for the largest part, with the two-step gas fuelling scheme as mentioned in section 2. Some changes in target recycling conditions may nevertheless still enter into play here, due to varying neutral deuterium content stored at the graphite tiles surface before each discharge, however the narrower  $p_{n,div}$  range obtained here suggests they play a minor role. With respect to [11], the absence of divertor baffles is translated into a higher slope for the  $n_{e,sep}-p_{n,div}$  correlation as well as an increase of the upstream separatrix density values overall. This is particularly evident when comparing the  $\delta_{up} \sim 0.4$  subset of discharges in the present work with the points in figure 5 (left)



of [11], within the 20–40 mPa  $p_{n,div}$  range. When considering the overall dataset, the  $\delta_{up}$  colormap suggests that the  $n_{e,sep}$  dependence on  $p_{n,div}$  is branched according to the upper triangularity value. More specifically, the separatrix density seemingly increases at similar  $p_{n,div}$  when moving from low to high plasma shaping, at least in the range  $\delta_{up} \gtrsim 0.2$ . In the opposite way, one can select a fixed value of  $n_{e,sep}$  at different upper triangularity, but this is accompanied by a variation of  $p_{n,div}$ .

This observation indicates that the properties of the SOL profiles may be sensitive not only to changes in plasma shaping in a direct way, but also to its indirect effects on other plasma parameters around the separatrix. This point is further supported by the variation of the  $\alpha_t$  parameter within  $\sim 0.5$  and  $\sim 1.5$ , displayed in figure 5(b), which is a larger range than that projected by the shaping-induced 1.6-fold increase by edge safety factor modification alone. More specifically, the upstream separatrix density range observed in figure 5(a) between  $\sim 1.5 \cdot 10^{19} \text{ m}^{-3}$  and  $\sim 2.1 \cdot 10^{19} \text{ m}^{-3}$  accounts for a further  $\sim 40\%$  increase in  $\alpha_t$ . While not shown here, a change in  $T_{e,sep}$  is also present, linked to both a broadening of the SOL power channel (see section 3.3) and a decrease of the power crossing the separatrix due to enhanced core radiation from low to high shaping, which is later discussed in section 5. The temperature decrease may be rather small, from  $\sim 48 \text{ eV}$  to  $\sim 42 \text{ eV}$ , however  $T_{e,sep}$  appears with a squared exponent in equation (1) so that a non-negligible  $\sim 30\%$  increase in  $\alpha_t$  must be taken into consideration. Finally, the role of  $Z_{eff}$ , which is also discussed more in detail in section 5, varies by  $\sim 20\%$  between  $\sim 1.6$  and  $\sim 1.9$ . Assuming that all these factors can be combined independently, one can estimate an approximate overall 3.5-fold increase in  $\alpha_t$ , similar to the 3.25 factor between the maximum and the minimum values.

### 3.3. Evolution of the divertor heat load profiles

Following the approach used in [11], the behaviour of the divertor heat load profiles has been investigated by means of the VIR thermography system. The infrared camera measures the floor tiles surface temperature distribution, which is then passed as input to the THEODOR code [53, 54] in order to solve a 1D heat conduction equation and yield the heat flux profile normal to the tiles surface. Accounting for target field line grazing angle and total flux expansion between the target and the OMP, an estimation of the upstream parallel heat flux profile is then obtained. After ELM-filtering (when possible) the measured heat load distribution in time, each individual profile is fitted with the exponential-diffusive model described in [55] to extract the relevant quantities. The upstream SOL power fall-off length  $\lambda_q$  within a given time interval is obtained by averaging the corresponding time-resolved series. The result is subsequently remapped to a poloidally averaged value by accounting for an average poloidal flux expansion factor as in equation (9) of [55]. Finally, the decay lengths are normalised to the so-called poloidal ion sound Larmor radius

$$\rho_{s,pol} = \frac{\sqrt{M_i T_{e,sep}}}{e \langle B_{pol} \rangle} \quad (3)$$

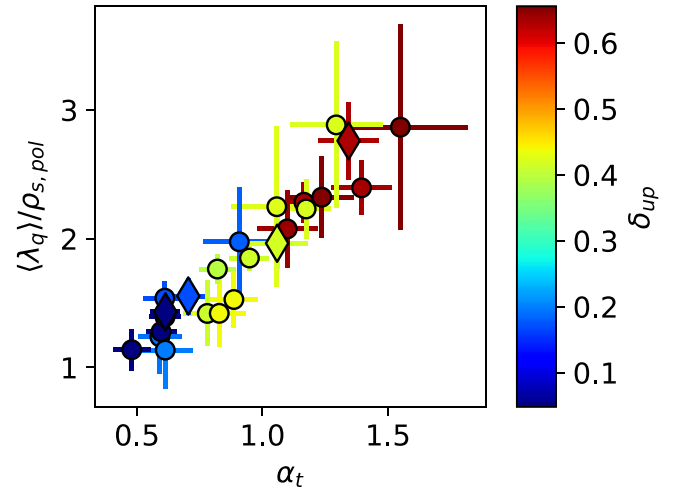


**Figure 6.** Modification of the normalised poloidally averaged SOL power fall-off length  $\langle \lambda_q \rangle / \rho_{s,pol}$  with respect to a change in upper triangularity and  $\alpha_t$  parameter. The colormap on the right is used to highlight different plasma shapes across the present dataset. The points corresponding to the profiles shown in figures 4 and 8 are shown as large diamonds.

where  $M_i$  is the effective ion mass and  $\langle B_{pol} \rangle$  is the poloidally averaged poloidal magnetic field. This normalisation is carried out in order to account for shaping-induced poloidal field variations and compare the results with the main reference scaling laws (e.g. [2, 56]).

The global result of this analysis across the present dataset is displayed in figure 6, showing evidence of a larger SOL power channel when moving towards high plasma shaping via an increase of the upper triangularity. In particular, an increase of  $\alpha_t$  produced by a higher shaping results in an increase of  $\langle \lambda_q \rangle / \rho_{s,pol}$  by a factor  $\sim 2.5$ . In physical units, this corresponds to a variation of  $\langle \lambda_q \rangle$  between  $\sim 10.6 \text{ mm}$  and  $\sim 27.2 \text{ mm}$ . This observation is coherent with the expected broadening of the divertor heat load profile from type-I ELMs to QCE H-modes. Furthermore, this increase does not take place sharply when moving from low to high shaping but rather gradually already at low  $\delta_{up}$ , hinting at a progressive destabilisation of resistive ballooning modes near the separatrix and pedestal bottom at increasing  $\alpha_t$ . Coherently with previous TCV [11] and AUG [5, 10] observations and further strengthening this interpretation, all the measured heat load widths are larger than the one predicted by a neoclassical heuristic-drift model [56, 57] for low collisionality type-I ELMs H-modes

$$\frac{\langle \lambda_q \rangle}{\rho_{s,pol}} \approx 1.6 \frac{a}{R_0} \quad (4)$$

which for TCV-like parameters is  $\sim 0.4$ .

In figure 7(a) comparison of the present results to those obtained within the gas scan database of [11] is shown. In the two datasets quantitatively similar ranges have been achieved in both the  $\alpha_t$  parameter and in the normalised SOL power width. The qualitative trends are quite resembling as well, with  $\langle \lambda_q \rangle / \rho_{s,pol}$  increasing by a similar amount in both cases. A

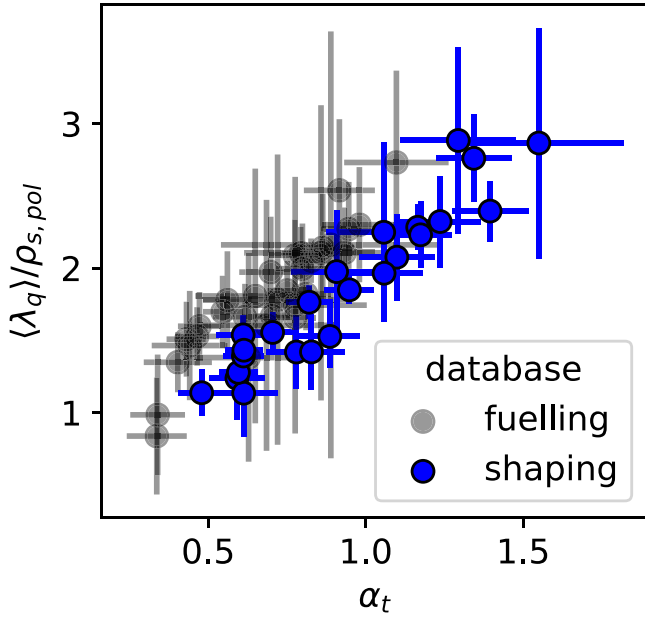


**Figure 7.** Comparison of the normalised  $\langle \lambda_q \rangle$  trends between the plasma shaping scan considered in this work (blue dots) and the gas fuelling scan published in [11] (transparent dots). The two datasets are characterised by quite similar qualitative trends and overall broadening within comparable  $\alpha_t$  ranges. The noticeable slight quantitative difference could be potentially ascribed to differences in diagnostics settings, calibration and analysis techniques which may be present between the two datasets.

slight discrepancy is however present, with one trend appearing shifted with respect to the other. This could potentially be attributed to small differences in the choice of analysis methods, for instance using the entire TS line of sight rather than the lower half only. Moreover, the plasma shaping database has been acquired several months after the gas scan experimental campaign, hence potentially introducing drifts in the calibration of some diagnostics like the VIR camera. Despite this difference, the close similarity in the two trends shown in figure 7 can represent a hint towards an unified description of the heat load profile evolution by means of the  $\alpha_t$  parameter.

### 3.4. Density profile modification

In this work the evolution of the upstream density profiles resulting from a change in plasma shaping is assessed both in the vicinity of the separatrix, where resistive ballooning transport originates, and further radially outwards in the far SOL. Figure 8 displays an example of this modification via a zoom on the edge–SOL part of the sample density profiles considered in section 3.1. The shown profiles have been normalised to their respective separatrix density, in order to highlight differences in their respective gradients and shape in the near and far SOL. Being characterised by similar  $n_{e, sep}$  values, any observable difference can be reliably attributed to the effect of plasma shaping. Indeed, the density profiles are visibly modified when moving from low to high upper triangularity. In particular, the near SOL gradient becomes progressively flatter

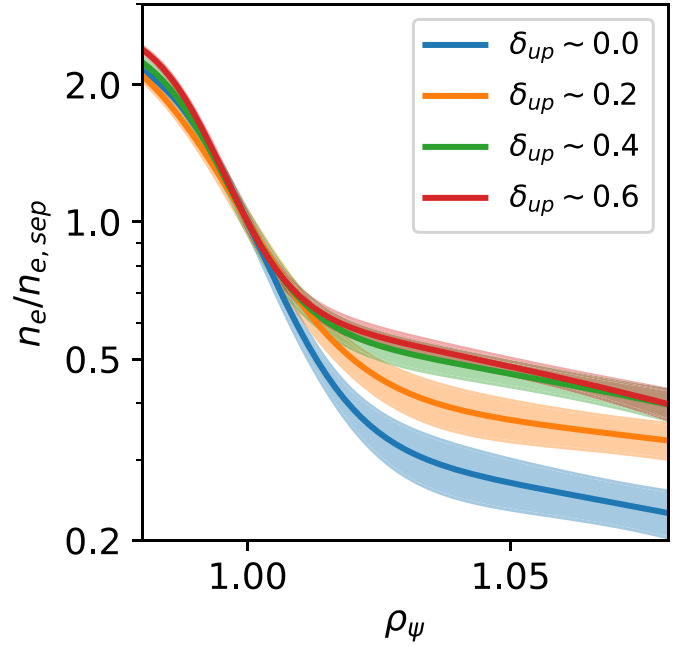


**Figure 8.** Upstream edge and scrape-off layer density profiles for the four sample discharges shown in figure 1, one for each shape, normalised to their respective separatrix density. All profiles are characterised by a similar separatrix density, so as to highlight differences due to plasma shaping alone. A logarithmic scale has been used on the y axis, in order to better highlight the development of a density shoulder feature as the plasma shape changes. For visualisation purposes, data points have been excluded from the plot.

and the distinct change in gradient between near and far SOL moves closer to the separatrix, resulting in a density shoulder forming in the far SOL.

Similar considerations can be made by examining the overall SOL density profile behaviour across the whole database, represented in the two panels of figure 9. On the one hand, the *mtanh* analytical fit can manage to well reproduce the main features of an H-mode profile. These include the pedestal top, the position and magnitude of the maximum pedestal gradient, as well as the separatrix position and the gross profile variation in the SOL. On the other hand, it sometimes fails at catching correctly the local near-SOL e-folding lengths, especially in QCE conditions when the profiles of the radial gradient may be strongly asymmetric about the maximum gradient radial coordinate [5]. For this reason an estimation of  $\lambda_n$  at the OMP has been attained in this work by fitting an exponential function to raw profile data in the radial range  $0 \leq R - R_{sep} \lesssim 10$  mm. Like with the SOL power decay length, the result has been subsequently remapped to poloidal average and normalised to  $\rho_{s, pol}$ . In figure 9(a), the normalised near-SOL density decay length exhibits a clear and continuous growth at increasing  $\alpha_t$  parameter, with greater gradient widths generally obtained at higher plasma shaping. The broadening of the near-SOL density profile amounts to a factor similar to the divertor heat load, from  $\sim 16.0$  mm to  $\sim 39.2$  mm in physical units for the poloidally-averaged decay length.

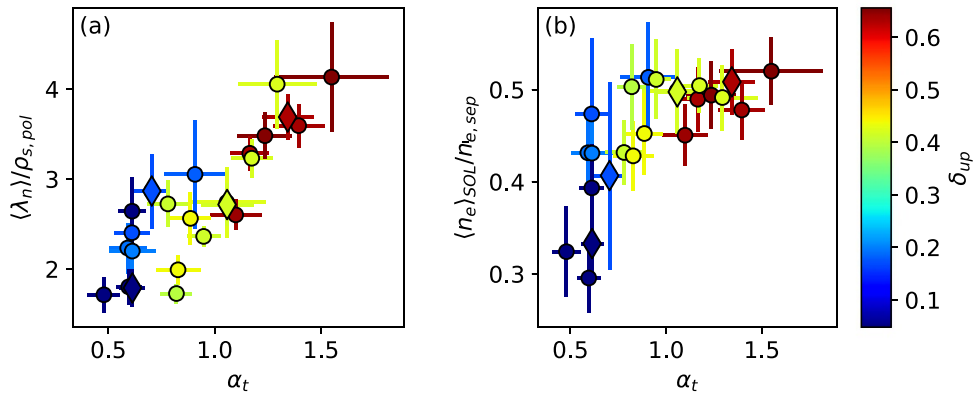


**Figure 9.** Modification of the normalised near-SOL density e-folding length (panel (a)) and density shoulder amplitude (panel (b)) across the scan in upper triangularity and  $\alpha_t$  parameter. The colormap on the right is used to distinguish different plasma shapes across the present dataset. In panel (a) the normalised near-SOL density e-folding length is calculated by fitting profile data with an exponentially decaying function from the separatrix up until  $R - R_{\text{sep}} \approx 10$  mm. The density shoulder amplitude qualifier of panel (b) is instead estimated over a radial range  $1.0 \leq \rho_{\psi} \leq 1.1$ , comprising both the near and far SOL regions. In both panels, the points corresponding to the profiles shown in figures 4 and 8 are shown as large diamonds.

For the purpose of characterising the global density profile behaviour, including the far SOL region, a density shoulder amplitude qualifier has been defined based on [11, 18] as the ratio between the radially averaged SOL density and the separatrix density:

$$\frac{\langle n_e \rangle_{\text{SOL}}}{n_{e,\text{sep}}} = \frac{1}{n_{e,\text{sep}}(\rho_{\psi,\text{max}} - 1)} \int_1^{\rho_{\psi,\text{max}}} n_e d\rho_{\psi}, \quad (5)$$

with  $\rho_{\psi,\text{max}} = 1.1$  for all discharges. In equation (5), at a difference with respect to [11, 18] the integral average has been calculated over the normalised poloidal flux coordinate  $\rho_{\psi}$  instead of the physical one  $R - R_{\text{sep}}$ . This choice allows to robustly account for flux expansion effects and changes in wall gap around the OMP introduced by modifications in plasma shaping. As illustrated in figure 9(b), the shoulder feature is more prominent for highly shaped plasmas, with its amplitude increasing with  $\alpha_t$  and saturating for  $\alpha_t \gtrsim 0.8$ . The two results shown in figure 9 support the interpretation according to which resistive ballooning modes become more unstable around the separatrix at higher plasma shaping through the reduction of local magnetic shear stabilisation, leading to greater radial particle transport and a broadening of the SOL density profile. The shoulder amplitude saturation takes place approximately for  $\alpha_t$  values around the onset of the QCE regime at high upper triangularity. This may signify that this mechanism is efficient in flattening the far-SOL gradients only up to full QCE establishment, after which the average SOL density increases proportionally to the separatrix density.

#### 4. Assessment of first wall density fluctuations

The increase in radial turbulent particle transport towards the first wall is believed to be the main cause of density shoulder formation moving from a type-I ELMy to a QCE regime.

Exploiting a fast reciprocating probe at the midplane, a correlation in TCV has already been reported [11] between a rise in resistive ballooning activity, triggered by a growing separatrix density, and an increase in filament radial velocity and size in high-density H-mode. In this work no direct measurements of the radial particle load were available during the experiments. Instead, the variations of density fluctuation properties with respect to the shaping are studied on the low-field side (LFS) midplane and first wall by means of wall-embedded LPs and THB data.

For the dataset introduced in section 2.2, no time-resolved fluctuation measurements were available, in particular since the wall-mounted LPs were run in swept mode with no constant bias phase. Therefore, dedicated plasma discharges have been run at the extreme  $\delta_{\text{up}}$  values, with the diagnostic setup shown in figure 10. The two shapes are represented by their separatrices as solid lines, whereas the two dotted contours indicate the first magnetic flux surfaces that intercept the outer first wall. The full set of wall-mounted LPs has been operated for these two discharges at constant negative bias voltage, in order to acquire time-resolved measurements of the ion saturation current. The same gas fuelling and heating schemes have been used as with the rest of the database, although for the discharge #76755 the duration of the NBI waveform has been halved due to operational restrictions. For both discharges, the same 300 ms long stationary time window has been taken into consideration, having again similar separatrix density at  $n_{e,\text{sep}} \sim 1.7 \cdot 10^{19} \text{ m}^{-3}$ . Given that no VIR camera measurements were available for these two discharges, the separatrix location and density have been estimated at the radial coordinate at which  $T_e \sim 45 \text{ eV}$ , corresponding to the temperature estimates in the previous section.

The normalised probability distribution function (PDF) of the inter-ELM  $j_{\text{sat}}$  signal is plotted in the top panel of figure 11 for the LP closest to the OMP, indicated in figure 10 as a white cross for each of the two geometries. This measurement has

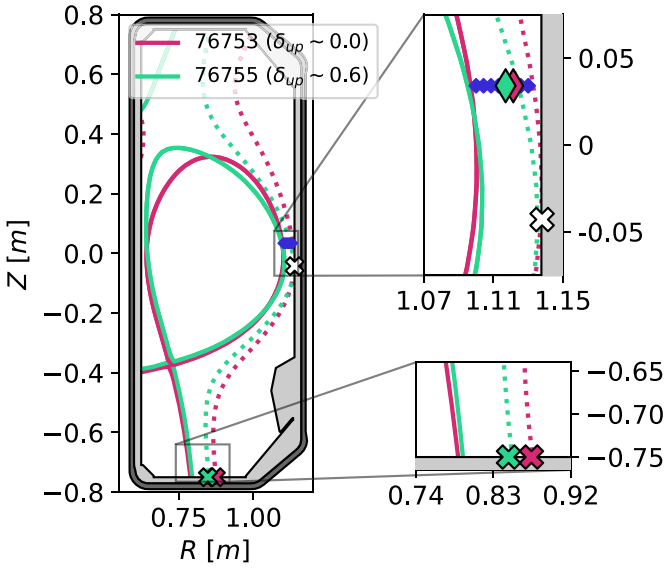


**Figure 10.** Layout of the edge-SOL diagnostics used to estimate first wall fluctuations, with a zoom-in on the outer midplane and divertor regions. The two considered geometries are represented by their separatrices as solid lines. The dotted lines indicate the first magnetic flux surfaces that intercept the LFS first wall for each shape. The white cross at the outer midplane and the two coloured ones at the divertor target pinpoint respectively the position of the midplane LP used for fluctuation analysis and the two probes magnetically connected to it. The blue diamonds near the midplane show the measurement positions of the THB diagnostic, with the selected channels represented by bigger markers of different colours.

been cross-compared with the HeI line emission at 667 nm as registered by one radial channel of the THB diagnostic. Its normalised PDF in the same time window as the midplane LP is shown in the bottom panel of the figure. In order to take into account the change in magnetic topology around the OMP introduced by the change in  $\delta_{up}$ , the THB channel showing the highest temporal correlation with respect to the midplane LP is chosen for each of the different shapes and indicated in figure 10 as coloured diamonds. For all PDFs the respective average values are represented by a dashed vertical line. The normalised PDFs in both panels are visibly affected when moving from low to high plasma shaping, with the average value increasing and the overall distribution exhibiting higher standard deviation and skewness. On the one hand, the observation of a higher average first wall  $j_{sat}$  signal at high shaping falls in line with the formation of a density shoulder and higher plasma density in QCE. On the other hand, the increased standard deviation and skewness are suggestive of an enhanced fluctuation level at high  $\delta_{up}$ . For both distributions, the marked positive skewness hints at the intermittent nature of far-SOL filamentary transport [58–61].

Figure 12 extends these observations by showing the full distribution of the  $j_{sat}$  average and standard deviation over the whole LFS first wall. Both quantities have been mapped, following TCV geometric conventions [62], on a curvilinear abscissa running clockwise around the tiles' perimeter and originating from the HFS midplane. Different portions of the LFS

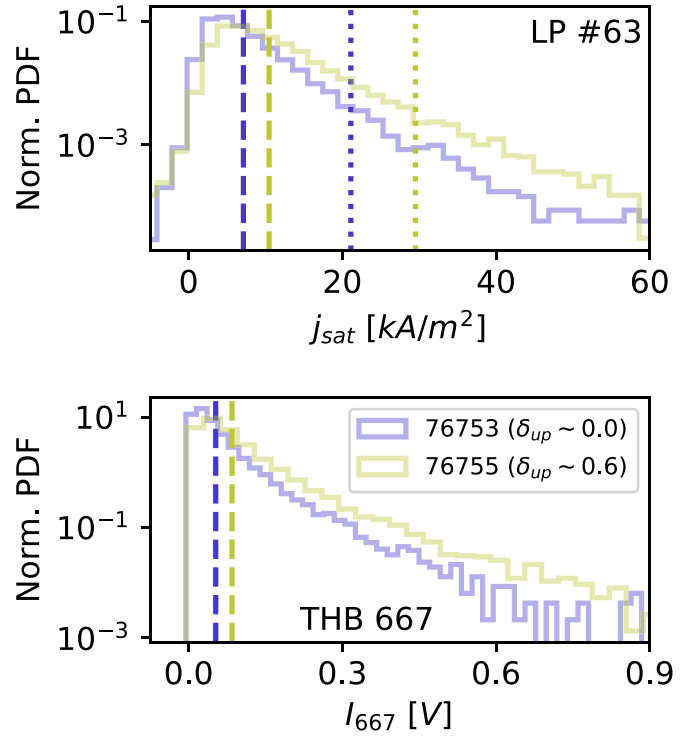


**Figure 11.** Top panel: normalised PDFs of the inter-ELM  $j_{sat}$  signals at the midplane Langmuir probe. Bottom panel: normalised PDFs of the 667 nm HeI line emission registered by a THB channel. For each shape, the THB channel with the highest temporal cross-correlation with respect to the midplane Langmuir probe signal is selected. Two PDFs are shown, each one corresponding to either the low shaping ( $\delta_{up} \sim 0$ , blue) or the high shaping ( $\delta_{up} \sim 0.6$ , yellow) case. In both panels, the dashed vertical lines indicate the PDF's average value. In the top panel, the dotted vertical lines represent the filament detection threshold as per equation (6).

first wall have been marked in the figure, being the upper and lower parts of the vertical tiles (respectively, above and below the OMP vertical coordinate) and the port protection tiles just above the vessel bottom-right corner. An increase of both the average and standard deviation of the  $j_{sat}$  first wall signals is visible on the lower vertical portion of the LFS first wall as  $\delta_{up}$  rises, with little change in the other poloidal regions. This suggests that an increase in turbulent activity takes place around and just below the OMP when moving towards high plasma shaping.

The filament detection frequency has been calculated both at the OMP probe and at divertor locations magnetically connected to it along the poloidal direction, marked in figure 10 as coloured crosses. Filaments appearing in the respective  $j_{sat}$  signals have been identified as all the peaks having an amplitude over the threshold defined by

$$j_{sat} \geq \langle j_{sat} \rangle + 2.5\sigma_{j_{sat}} \quad (6)$$

where the background component  $\langle j_{sat} \rangle$  and the standard deviation  $\sigma_{j_{sat}}$  of the ion saturation current density have been estimated via a moving window of 0.2 ms width. This threshold is shown in figure 11 as dotted lines superimposed to the



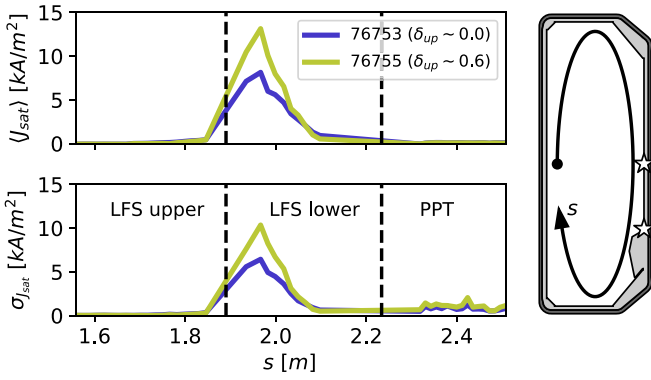


**Figure 12.** Distribution of the average (top left) and standard deviation (bottom left) of the inter-ELM  $j_{\text{sat}}$  signals calculated for the LFS first wall Langmuir probes within the considered time window. The horizontal coordinate  $s$  corresponds to a curvilinear abscissa running clockwise along the tiles' perimeter, starting from the HFS midplane. This curvilinear abscissa is visualised on the TCv poloidal cross section on the right, with the direction marked by the elliptical arrow. The inspected sections comprise both the upper and the lower part of the LFS first wall, including the port protection tiles (PPTs) near the lower-right corner of the vacuum vessel. The boundaries between different sections are marked as dashed lines in the two left plots, and as white stars in the TCv poloidal cut on the right.

midplane LP distribution functions. An estimate of the filament frequency for the two different shapes is given in figure 13, where the symbols and the boxplots represent respectively the time average and the dispersion of frequency data within the considered time window. At the OMP the filament frequency is seen to clearly increase with shaping, or equivalently with  $\alpha_t$ . This observation supports the idea of an enhanced ballooning activity near the separatrix at higher upper triangularity, leading to a greater number of filaments being expelled into the SOL. Conversely, the filamentary dynamics at the divertor target seems to not be greatly affected by the change in shape, with both the frequency average, median and dispersion seemingly unchanged. This information could indicate that midplane filaments are unable to reach the divertor target, which may be due to high divertor collisionality or flux flaring around the poloidal field null [60, 63]. Nevertheless, it cannot be excluded in this work that they reach at least partially into the divertor region, like observed in TCv high density L-mode plasmas [64]. Divertor-localised filaments could provide in part another possible interpretation, originating below the X-point itself and being therefore decorrelated from the upstream fluctuations [65].

## 5. Plasma-wall interaction issues

The results shown in the previous sections have highlighted the prominent role of plasma shaping in setting the SOL properties, which reflects on both upstream profiles modifications and changes in fluctuation properties at the OMP. However, part of the observed behaviour could still be potentially ascribed to indirect effects of shaping changes on other

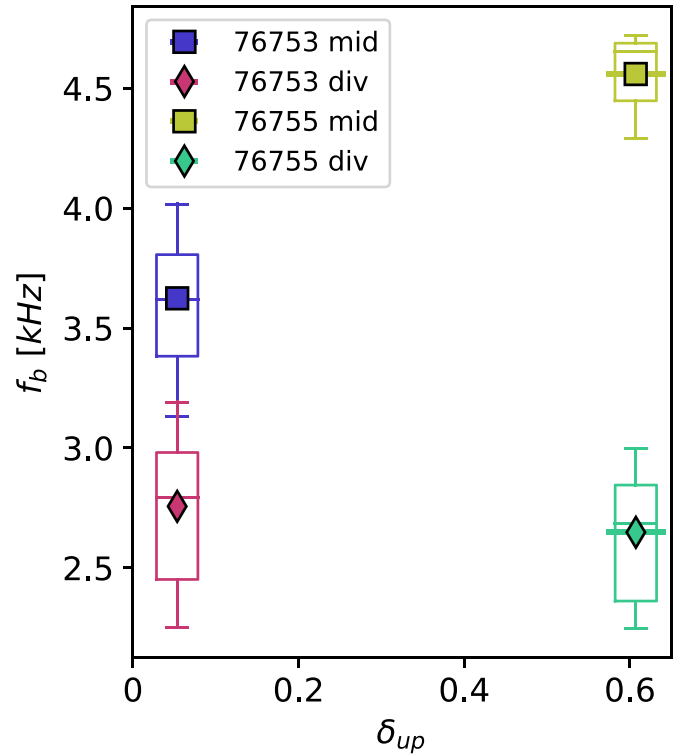


**Figure 13.** Change in filament frequency with upper triangularity as detected from the midplane and divertor target Langmuir probes. The boxplots provide an indication of the frequency data dispersion, with the horizontal line at the centre being the median and the box vertical boundaries indicating the inter-quartile range. The squares and diamonds, superimposed to the boxplots, represent the average filament detection frequency within the considered time window for the probes located at, respectively, the midplane and the outer target, with the horizontal error bars denoting the uncertainty on  $\delta_{\text{up}}$ .

plasma parameters. In section 3, for instance, a possible correlation has emerged between the upper triangularity and the upstream separatrix density at similar levels of divertor neutral pressure. Furthermore, other experimental efforts focusing on TCv L-mode plasmas have brought forward the influence of plasma geometry (as well as the degree of divertor closure) on midplane neutral pressure and particle sources [19]. In particular, the highly shaped plasmas in this work are associated to a smaller outer gap and a much closer to double null magnetic field configuration. This could lead to modifications in the recycling sources at the OMP as well as on the carbon impurity intake from the first wall, potentially affecting also the profiles and the transport level. Under these circumstances, clearing the role played by the shape on plasma-wall interaction properties and first wall recycling is a crucial task.

In order to carry out this evaluation, data from the midplane baratron gauge has been considered. Figure 14 displays the time evolution of the midplane neutral pressure, as estimated by the the midplane baratron gauge, for two samples discharges within the database considered in section 3. The pressure time traces have been pre-treated by applying a band-pass digital filter between 12 and 24 Hz, with the purpose of eliminating fast oscillations in the raw signal. The time trace



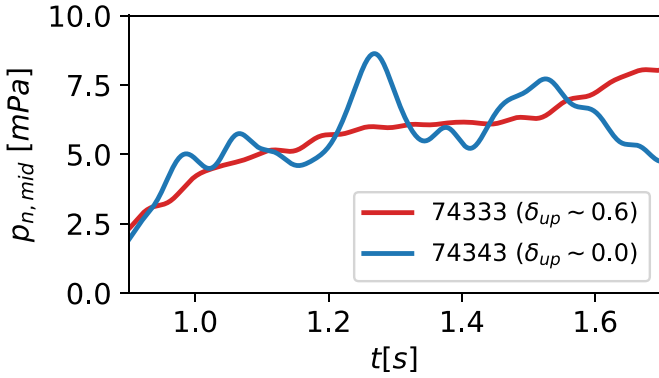


**Figure 14.** Time evolution of the filtered neutral pressure as measured by the midplane baratron gauge, for two discharges having the highest (red) and lowest (blue) upper triangularity.

for the low  $\delta_{up}$  discharge 74343 shows larger variation than for the high  $\delta_{up}$  case 74333, which may be due to the finite time response of the baratron gauge causing a smoothing of fast excursions in the  $p_{n,mid}$  signal induced by ELM activity. Despite this, it can be seen that the two traces stay relatively close to each other throughout the entirety of the H-mode phase represented in the figure, indicating that a change in shaping has a negligible effect on the upstream neutral density. Variations in the local ionisation sources, contributing to the far SOL density, would then be affected only by the increase in turbulent activity leading to the formation of a density shoulder at high shaping. It must be stressed out that the midplane baratron is mounted on a long extension tube ending outside the toroidal field coils, therefore its measurement may differ from the actual in-vessel neutral pressure even by an order of magnitude. Simple 0D models could be used like the one by Niemczewski [66] relating the first wall pressure with the gauge-measured pressure, however in this work it cannot be applied due to the lack of necessary data such as the neutral temperature at the tube entrance. Regardless of the experimental observations reported here, it is worth noting that enough energy must be transported into the SOL in order to ionise the neutrals and promote a local increase of the far SOL density profile, as for example highlighted through numerical work on AUG [67]. Consequently, even in the presence of a higher neutral population density, which is anyway not observed in figure 14, the ionisation level required for the density shoulder to form at high shaping can be ensured only by an enhancement in turbulent transport level such as that seen in section 4.

The change in magnetic topology can nonetheless have measurable effects on the main plasma radiative losses, as anticipated in section 2. Figure 15 illustrates two emissivity maps for the discharges 76753 and 76755, one for each extreme upper triangularity value, obtained by tomographic inversion of RADCAM bolometry data. The temporal evolution of the total power radiated from the confined plasma  $P_{rad,core}$  is represented in the bottom panel. The two emissivity maps show that the highly shaped equilibrium is associated with more significant core radiative losses. Greater carbon

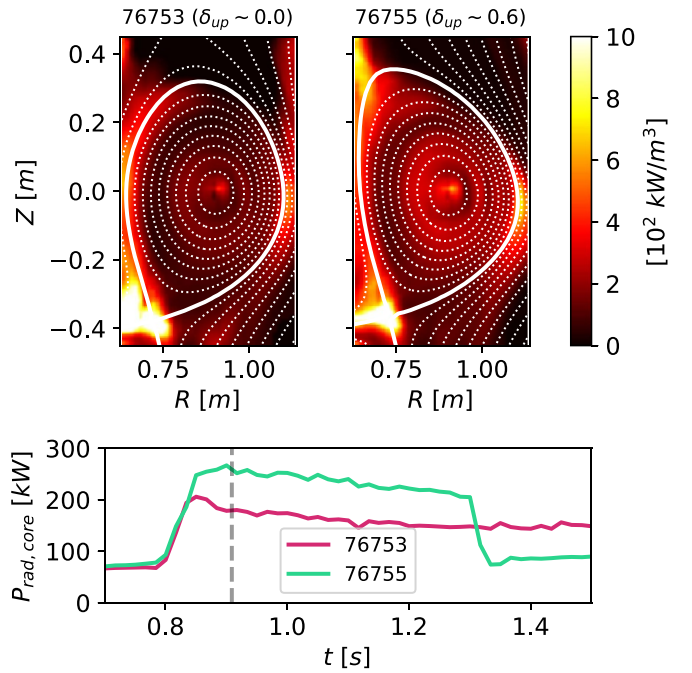


**Figure 15.** Top panels: emissivity maps computed by tomographic inversion of RADCAM data at a time frame around  $\sim 0.91$  s for plasma discharges 76753 (low shaping) and 76755 (high shaping). In order to better highlight differences in core radiation, the colourbar has been saturated at  $1 \text{ MW m}^{-3}$ . Bottom panel: time evolution of the total power radiated from the confined region for the two discharges. The vertical dashed line indicates the time instant at which the two emissivity maps of the top panels are plotted.

intake from the first wall at high  $\delta_{up}$  may be responsible for this, since the effective ion charge (measured as indicated in section 3.1) is estimated to be  $Z_{eff} \sim 1.6$  for the low shaping pulse and  $Z_{eff} \sim 1.9$  for the high shaping pulse. This variation may be owed to the larger density fluctuation level coupled with a smaller outer gap, leading to a more intense plasma-wall interaction at the OMP. In addition, the close-to-double-null configuration in the highly shaped case with a secondary X-point quite close to the main separatrix may lead to an additional impurity source term from the machine roof tiles. As demonstrated by the  $P_{rad,core}$  time trace in the bottom panel of figure 15, this behaviour is observable during the whole duration of the H-mode phase and leads to an additional  $\sim 80$  kW of radiated power from the lowest to the highest  $\delta_{up}$  values. This variation has inevitably repercussions on the SOL power balance by decreasing  $P_{sep}$  by an equal amount. Nevertheless, the resulting  $T_{e,sep}$  reduction is much less significant, due to the dominant contribution of the NBI input power as well as the  $2/7$  exponent in equation (2).

## 6. Conclusions and outlook

A set of high density H-mode discharges has been obtained on the TCV tokamak with the purpose of studying the effect of plasma shaping on SOL profiles and transport. The magnetic equilibrium geometry has been varied from shot to shot by

changing the upper triangularity in a wide range of values at constant plasma current, toroidal magnetic field, heating and gas fuelling schemes. While a clear type-I ELM regime is visible at low shaping, a transition to QCE takes place at high shaping with low amplitude, frequent, incoherent fluctuations appearing instead of well-defined periodic bursts. This observation supports previous analysis and modelling results [6, 7] according to which high shaping is associated with the generation of small ELMs via a reduction of the stabilising effect of magnetic shear on ballooning modes near the separatrix.

Like in [11], the evolution of the upstream profiles and transport properties has been parametrised in terms of the  $\alpha_t$  turbulence control parameter, introduced in [10]. While a large part of the achieved  $\alpha_t$  variation can be ascribed to the change in upper triangularity and associated edge safety factor, the covariance of other parameters with the plasma shaping has been seen to play a significant role in its determination. In the near SOL both the parallel heat load and the density profiles have been seen to undergo a significant broadening, with their e-folding lengths increasing by a factor  $\sim 2.5$  across the spanned  $\delta_{up}$  and  $\alpha_t$  intervals. Notably, the trend shown in this work by the heat load width with respect to  $\alpha_t$  follows closely the one shown in [11] obtained via a gas-fuelling induced  $n_{e,sep}$  scan, at least on a qualitative side. While small quantitative deviations could be likely explained in terms of differences in diagnostics settings or calibration, this point further strengthens the interpretation of  $\alpha_t$  being a key parameter in controlling the amount of SOL particle and heat transport. In the far SOL, similarly to other previous L- and H-mode experiments, a shoulder develops when moving towards high  $\alpha_t$  and into the QCE boundaries, with the shoulder amplitude as defined in equation (5) eventually saturating for  $\alpha_t \gtrsim 0.8$ .

Moving from low to high shaping, also the turbulent fluctuation level around the midplane undergoes significant modifications, highlighted by exploiting the full set of wall-mounted LPs. The PDF of the ion saturation current signal acquired by a midplane probe is characterised by a greater average value and a more significant spread at high upper triangularity. This observation is not limited to the midplane only, but rather it involves a significant part of the LFS first wall. Moreover, the measured PDFs are strongly positively skewed, denoting the intermittent filamentary nature of the far SOL turbulent fluctuations. The frequency of these filaments has been demonstrated to increase at the midplane when moving from low to high plasma shaping, whereas no significant change has been observed on the divertor probes. These observations can serve as a possible indication of an increasing radial turbulent particle flux when moving from low to high plasma shaping. It is worth highlighting that the latter statement is only suggestive and cannot be directly drawn from the analysis presented in this work. Indeed, proper measurements of the first wall particle load are lacking in this manuscript and would be desirable for future experimental work.

The role of plasma shaping in setting SOL particle sources and plasma-wall interaction characteristics has also been investigated. The midplane neutral pressure as measured by a baratron gauge shows little variation with plasma shaping,

hinting at a negligible effect of the latter on first wall recycling sources and neutral density. The modification of the density profiles, with formation of a far SOL shoulder at high  $\delta_{up}$ , could then be likely ascribed at leading order to the changes in turbulent dynamics caused by the variation in plasma shaping. In any case, even if more neutrals were indeed present because of enhanced first wall recycling sources, enough energy must be transported radially outwards for these neutrals to be actually ionised. At constant input power, this condition can only be met under the assumption of an enhancement in the cross-field transport level, such as that indicated by the experimental observations made in this work when moving from low to high shaping. Higher core radiative losses have been registered as well at high  $\delta_{up}$ , linked to a more significant carbon impurity intake from the first wall. The higher turbulence level and resulting more intense plasma-wall interaction may be partly responsible for this. In addition, the magnetic topology may provide a further contribution through a smaller outer gap at the midplane, as well as the close-to-double-null configuration at high shaping providing a further impurity source from the roof tiles.

The previously described experimental results, together with previous TCV [11] and AUG [5, 10, 33] findings, all point towards an interpretation of the SOL dynamics as being governed by resistive ballooning turbulence in high density H-mode conditions. On this line, the  $\alpha_t$  parameter theoretical framework represents a promising tool in providing a description of the SOL profiles and transport properties. Intense international experimental efforts are currently underway on other European fusion research devices in order to attempt an extension of this description on a multi-machine basis.

## Acknowledgments

This work has been carried out within the framework of the EUROfusion Consortium, partially funded by the European Union via the Euratom Research and Training Programme (Grant Agreement No. 101052200—EUROfusion). The Swiss contribution to this work has been funded by the Swiss State Secretariat for Education, Research and Innovation (SERI). Views and opinions expressed are however those of the author(s) only and do not necessarily reflect those of the European Union, the European Commission or SERI. Neither the European Union nor the European Commission nor SERI can be held responsible for them. This work was supported in part by the Swiss National Science Foundation, and in part by the US Department of Energy under Award No. DE-SC0010529.

## ORCID iDs

A. Stagni  <https://orcid.org/0000-0001-8084-1544>  
 N. Vianello  <https://orcid.org/0000-0003-4401-5346>  
 M. Agostini  <https://orcid.org/0000-0002-3823-1002>  
 S. Gorno  <https://orcid.org/0000-0003-0524-7283>  
 B. Labit  <https://orcid.org/0000-0002-0751-8182>

U. Sheikh  <https://orcid.org/0000-0001-6207-2489>  
 M. Ugoletti  <https://orcid.org/0000-0002-7498-0780>  
 Y. Wang  <https://orcid.org/0009-0004-5888-2277>  
 C. Wüthrich  <https://orcid.org/0000-0001-7548-2452>  
 J.A. Boedo  <https://orcid.org/0000-0003-2230-4112>  
 H. Reimerdes  <https://orcid.org/0000-0002-9726-1519>  
 C. Theiler  <https://orcid.org/0000-0003-3926-1374>

## References

- [1] Pitts R. et al 2019 *Nucl. Mater. Energy* **20** 100696
- [2] Eich T. et al 2013 *Nucl. Fusion* **53** 093031
- [3] Sips A. et al 2018 *Nucl. Fusion* **58** 126010
- [4] Zohm H. 1996 *Plasma Phys. Control. Fusion* **38** 1213
- [5] Faitsch M., Eich T., Harrer G., Wolfrum E., Brida D., David P., Griener M. and Stroth U. 2021 *Nucl. Mater. Energy* **26** 100890
- [6] Harrer G. et al 2018 *Nucl. Fusion* **58** 112001
- [7] Labit B. et al 2019 *Nucl. Fusion* **59** 086020
- [8] Stober J., Maraschek M., Conway G., Gruber O., Herrmann A., Sips A., Treutterer W. and Zohm H. 2001 *Nucl. Fusion* **41** 1123–34
- [9] Saibene G. et al 2005 *Nucl. Fusion* **45** 297
- [10] Eich T., Manz P., Goldston R., Hennequin P., David P., Faitsch M., Kurzan B., Sieglin B. and Wolfrum E. 2020 *Nucl. Fusion* **60** 056016
- [11] Stagni A. et al (the TCV Team and the EUROfusion MST1 Team) 2022 *Nucl. Fusion* **62** 096031
- [12] Goldston R.J., Reinke M.L. and Schwartz J.A. 2017 *Plasma Phys. Control. Fusion* **59** 055015
- [13] LaBombard B., Boivin R.L., Greenwald M., Hughes J., Lipschultz B., Mossessian D., Pitcher C.S., Terry J.L. and Zweben S.J. 2001 *Phys. Plasmas* **8** 2107–17
- [14] Rudakov D. et al 2005 *Nucl. Fusion* **45** 1589–99
- [15] Garcia O., Horacek J., Pitts R., Nielsen A., Fundamenski W., Naulin V. and Rasmussen J.J. 2007 *Nucl. Fusion* **47** 667–76
- [16] Carralero D., Artene S., Bernert M., Birkenmeier G., Faitsch M., Manz P., de Marne P., Stroth U., Wischmeier M. and Wolfrum E. 2018 *Nucl. Fusion* **58** 096015
- [17] Vianello N. et al 2020 *Nucl. Fusion* **60** 016001
- [18] Février O. et al 2020 *Plasma Phys. Control. Fusion* **62** 035017
- [19] Tsui C.K. et al 2022 *Phys. Plasmas* **29** 062507
- [20] Müller H., Bernert M., Carralero D., Kallenbach A., Kurzan B., Scarabosio A., Sieglin B., Tophøj L., Vianello N. and Wolfrum E. 2015 *J. Nucl. Mater.* **463** 739–43
- [21] Carralero D. et al 2017 *Nucl. Mater. Energy* **12** 1189–93
- [22] Vianello N. et al (the ASDEX Upgrade team, the TCV team, the EUROfusion MST1 team and the JET Contributors) 2021 SOL profile and fluctuations in different divertor recycling conditions in H-mode plasmas 2020 *IAEA Fusion Energy Conf. (NICE)* [EX/P3-14]
- [23] Griener M. et al 2020 *Nucl. Mater. Energy* **25** 100854
- [24] Redl A. et al (the ASDEX Upgrade team and the EUROfusion MST1 team) 2023 An extensive analysis of SOL properties in high- $\delta$  plasmas in ASDEX Upgrade *Nucl. Fusion* submitted
- [25] Harrer G.F. et al (the ASDEX Upgrade Team and the EUROfusion MST1 Team) 2022 *Phys. Rev. Lett.* **129** 165001
- [26] Radovanovic L., Dunne M., Wolfrum E., Harrer G., Faitsch M., Fischer R. and Aumayr F. (the ASDEX Upgrade Team and the EUROfusion MST1 Team) 2022 *Nucl. Fusion* **62** 086004
- [27] Eich T. and Manz P. (the ASDEX Upgrade team) 2021 *Nucl. Fusion* **61** 086017
- [28] Rogers B.N., Drake J.F. and Zeiler A. 1998 *Phys. Rev. Lett.* **81** 4396–9
- [29] Scott B.D. 2005 *Phys. Plasmas* **12** 062314
- [30] Scott B.D. 2007 *Plasma Phys. Control. Fusion* **49** S25–S41
- [31] Scott B.D. 2002 *New J. Phys.* **4** 52–52
- [32] Hohmann T., Redl A., Rohde V., Schall G. and Schandrud M. 2023 *Fusion Eng. Des.* **187** 113365
- [33] Redl A., Eich T., Vianello N. and David P. 2023 *Nucl. Mater. Energy* **34** 101319
- [34] Hofmann F. et al 1994 *Plasma Phys. Control. Fusion* **36** B277
- [35] Bates S.C. and Burrell K.H. 1984 *Rev. Sci. Instrum.* **55** 934–9
- [36] Kruezi U., Sergienko G., Morgan P.D., Matthews G.F., Brezinsek S. and Vartanian S. (JET-EFDA Contributors) 2012 *Rev. Sci. Instrum.* **83** 10D728
- [37] Hawke J. et al 2017 *J. Instrum.* **12** C12005–12005
- [38] Maurizio R., Elmore S., Fedorczak N., Gallo A., Reimerdes H., Labit B., Theiler C., Tsui C. and Vijvers W. 2018 *Nucl. Fusion* **58** 016052
- [39] Février O., Theiler C., De Oliveira H., Labit B., Fedorczak N. and Baillod A. 2018 *Rev. Sci. Instrum.* **89** 053502
- [40] De Oliveira H., Marmillod P., Theiler C., Chavan R., Février O., Labit B., Lavanchy P., Marlétaz B. and Pitts R.A. 2019 *Rev. Sci. Instrum.* **90** 083502
- [41] Agostini M., Scarin P., Cavazzana R., Carraro L., Grandò L., Taliere C., Franchin L. and Tiso A. 2015 *Rev. Sci. Instrum.* **86** 123513
- [42] Agostini M., Scarin P., Milazzo R., Cervaro V. and Ghiraldelli R. 2020 *Rev. Sci. Instrum.* **91** 113503
- [43] Karpushov A.N. et al 2017 *Fusion Eng. Des.* **123** 468–72
- [44] Sheikh U.A., Simons L., Duval B.P., Février O., Moret D., Allegrucci A., Bernert M., Crisinel F., Tersztyánszky T. and Villingier O. 2022 *Rev. Sci. Instrum.* **93** 113513
- [45] Frassinetti L. et al (JET Contributors) 2020 *Nucl. Fusion* **61** 016001
- [46] Maurizio R., Duval B., Labit B., Reimerdes H., Faitsch M., Komm M., Sheikh U. and Theiler C. (the TCV team) 2021 *Nucl. Fusion* **61** 024003
- [47] Stangeby P., Canik J., Elder J., Lasnier C., Leonard A., Eldon D., Makowski M., Osborne T. and Grierson B. 2015 *Nucl. Fusion* **55** 093014
- [48] Sauter O., Angioni C. and Lin-Liu Y.R. 1999 *Phys. Plasmas* **6** 2834–9
- [49] Sauter O., Angioni C. and Lin-Liu Y.R. 2002 *Phys. Plasmas* **9** 5140–5140
- [50] Sheikh U.A., Dunne M., Frassinetti L., Blanchard P., Duval B.P., Labit B., Merle A., Sauter O., Theiler C. and Tsui C. 2018 *Plasma Phys. Control. Fusion* **61** 014002
- [51] Stober J., Gruber O., Kallenbach A., Mertens V., Ryter F., Stäbler A., Suttrop W. and Treutterer W. (the ASDEX Upgrade Team) 2000 *Plasma Phys. Control. Fusion* **42** A211
- [52] Saibene G. et al 2002 *Plasma Phys. Control. Fusion* **44** 1769
- [53] Herrmann A., Junker W., Gunther K., Bosch S., Kaufmann M., Neuhauser J., Pautasso G., Richter T. and Schneider R. 1995 *Plasma Phys. Control. Fusion* **37** 17–29
- [54] Sieglin B., Faitsch M., Herrmann A., Brucker B., Eich T., Kammerloher L. and Martinov S. 2015 *Rev. Sci. Instrum.* **86** 113502
- [55] Eich T., Sieglin B., Scarabosio A., Fundamenski W., Goldston R.J. and Herrmann A. (the ASDEX Upgrade Team) 2011 *Phys. Rev. Lett.* **107** 215001
- [56] Goldston R. 2012 *Nucl. Fusion* **52** 013009
- [57] Goldston R. 2015 *J. Nucl. Mater.* **463** 397–400
- [58] Boedo J.A. et al 2001 *Phys. Plasmas* **8** 4826–33
- [59] Boedo J.A. et al 2003 *Phys. Plasmas* **10** 1670–7
- [60] D'Ippolito D.A., Myra J.R. and Zweben S.J. 2011 *Phys. Plasmas* **18** 060501

- [61] Kuang A., LaBombard B., Brunner D., Garcia O., Kube R. and Theodorsen A. 2019 *Nucl. Mater. Energy* **19** 295–9
- [62] Moret J.M., Buhlmann F., Fasel D., Hofmann F. and Tonetti G. 1998 *Rev. Sci. Instrum.* **69** 2333–48
- [63] Myra J.R., Russell D.A. and D'Ippolito D.A. 2006 *Phys. Plasmas* **13** 112502
- [64] Offeddu N. *et al* (the TCV Team) 2022 *Nucl. Fusion* **62** 096014
- [65] Wüthrich C. *et al* (the TCV Team) 2022 *Nucl. Fusion* **62** 106022
- [66] Niemczewski A. 1995 Neutral particle dynamics in the Alcator C-mod tokamak *PhD Thesis* Massachusetts Institute of Technology
- [67] Zito A., Wischmeier M., Carralero D., Manz P., Pérez I.P. and Passoni M. (the ASDEX Upgrade Team) 2021 *Plasma Phys. Control. Fusion* **63** 075003